CHEMISTRY OF MATERIALS

pubs.acs.org/cm

Article

Structure, Second-, and Third-Harmonic Generation of $Li_4P_2S_6$: A Wide Gap Material with a High Laser-Induced Damage Threshold

Benjamin M. Oxley, Kyeong-Hyeon Lee, Thomas S. Ie, Jae Mo Lee, Michael J. Waters, James M. Rondinelli, Joon I. Jang,* and Mercouri G. Kanatzidis*

Cite This: *Chem. Mater.* 2023, 35, 7322–7332

Read Online

ACCESS | Metrics & More | Article Recommendations | Supporting Information

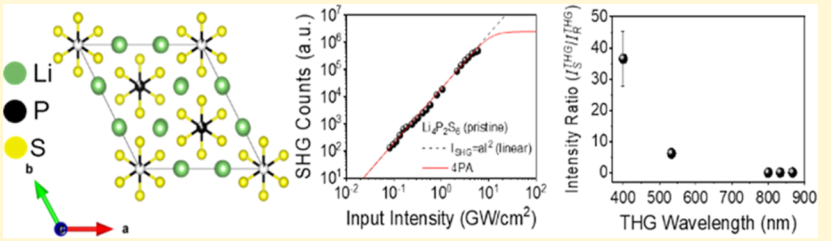

ABSTRACT: $Li_4P_2S_6$ is a Li-rich, wide bandgap (3.74 eV) material that has been extensively studied for use in solid-state batteries. We offer a further examination and report here the first single-crystal structure determination with a special emphasis on its nonlinear optical (NLO) properties. $Li_4P_2S_6$ crystallizes in the *P*321 space group in a zero-dimensional (0-D) structure, with molecular $[P_2S_6]^{4-}$ units surrounded by a noncentrosymmetric Li^+ net. $Li_4P_2S_6$ does not melt up to 700 °C but instead thermally decomposes at 641 °C in air, off-gassing a combination of H_2S, S (measured as S_2 and S_3), and $H_2P_2S_4$. Upon cooling, there is a thermal event at 387 °C, likely due to the recondensation of volatile species. $Li_4P_2S_6$ is air-stable in dry conditions despite a very high Li-content; however, it fully decomposes in sufficiently humid environments. Second-harmonic generation (SHG), third-harmonic generation (THG), and laser-induced damage threshold (LIDT) data were measured for $Li_4P_2S_6$. It was found to have a moderate SHG intensity (~0.1 × $AgGaSe_2$), but an exceptional LIDT due to its wide bandgap, outperforming $AgGaSe_2$ by a factor of almost 16. $Li_4P_2S_6$ was found to have moderate THG intensity (~0.2 × $AgGaSe_2$) at energies below the bandgap of the reference, but exceptional THG intensity (~36 × $AgGaSe_2$) at higher energies where the reference self-absorbs THG output. $Li_4P_2S_6$ is an excellent material for high-power NLO applications, especially for the efficient conversion of infrared (IR) to visible via THG and potentially other third-order NLO processes.

INTRODUCTION

$Li_4P_2S_6$ is a zero-dimensional (0-D) material consisting of staggered ethane-like $[P_2S_6]^{4-}$ units that are fully separated by a Li^+ net. Li-rich materials such as this are good candidates for solid-state electrolytes, and in fact, $Li_4P_2S_6$ and the related Li_2S-P_2S_5 glass have been studied electrolytically as candidates for battery materials.[1,2] These studies find that the ionic conductivity of the Li_2S-P_2S_5 glass is much higher than that of the crystalline $Li_4P_2S_6$, presumably due to the greater degree of freedom in the bonding motifs, but there have been no single-crystal structure determinations of $Li_4P_2S_6$ that definitively assign the coordination environment around the Li^+ atoms. The first report of the material by Mercier et al. describes $Li_4P_2S_6$ in the $P6_3/mcm$ space group as columns of 50% occupied P atoms trigonally coordinated to S, with 1 Li site between the chains to maintain charge balance (Figure S1a,f).[3] Following studies use Mercier's synthetic method of either devitrifying glassy $Li_4P_2S_7$ at high temperatures, driving off excess S to yield crystalline $Li_4P_2S_6$, or by stoichiometrically combining Li_2S, P, and S at 900 °C for 1 h and then thermally annealing at 450 °C for 16 h. These methods yield small (>10 μm) particles, unsuitable for single-crystal diffraction studies.[4] As a result, structural studies using these synthetic methods rely on high-energy powder diffraction studies and Rietveld refinements, yielding conflicting space groups. The currently reported space groups of $Li_4P_2S_6$ in the ICSD as of June 2023 are $P6_3/mcm$, $P\bar{3}1m$, and *P*321, almost all of which used synchrotron X-ray or neutron powder diffraction experiments to determine the structure.[1,3,5] Fully understanding a material's structure is paramount for discovering its practical applications, especially when a number of properties require noncentrosymmetry.

Our group has extensively studied noncentrosymmetric low-dimensional materials to gain insights into the underlying

Received: July 17, 2023
Revised: August 4, 2023
Published: August 31, 2023

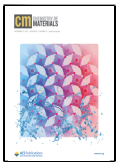

structure−property relationships behind NLO properties such as SHG and THG.[6−8] Here, we define dimensionality as the number of crystallographic axes in which there is long-range covalent bonding. In particular, we found that the one-dimensional (1-D) family $AAsQ_2$ (A = Li, Na, K; and Q = S, Se) has some of the highest SHG outputs in the IR to date (648 pm/V for γ-$NaAs_{0.95}Sb_{0.05}Se_2$)[9−15] and that the two-dimensional (2-D) family $AGaM'Q_4$ (A = K, Rb, Cs, Tl; M′ = Ge, Sn; and Q = S, Se) outperforms the THG of industry-standard material $AgGaS_2$ by up to four times.[16] Theoretical studies on the chalcoarsenates show that the reduced dimensionality leads to a high degree of separation between adjacent chain orbitals, flattening the electronic bands and increasing the overall nonlinear response.[13] This begets our hypothesis that 0-D materials should have even higher nonlinear responses because each polarizable unit is fully isolated from its neighbor. To date, there are few reports of second-harmonic responses from 0-D noncentrosymmetric chalcogenides. Each of these 0-D materials exhibits outstanding responses: $Ba_8Sn_4S_{15}$ (SHG ∼10 × $AgGaS_2$) and $Ba_{23}Ga_8Sb_2S_{38}$ (SHG ∼22 × $AgGaS_2$).[17,18] In fact, Chen et al. attributed the high response of $Ba_{23}Ga_8Sb_2S_{38}$ to the separation of the GaS_4 units, and the band structure of $Ba_8Sn_4S_{15}$ shows almost perfectly flat non-dispersing valence and conduction bands. Based on these reports, targeting additional 0-D materials will give us greater insight into the origins of the correlation between dimensionality and SHG.

Harmonic generation results from a material's nonlinear polarization under light. It employs an intermediate virtual level to instantly double or triple photon frequencies.[19] SHG and THG are utilized for important applications such as optical microscopy of biological tissue,[20] advances in the fundamental understanding of nanostructures,[21] and the creation of novel solid-state lasing wavelengths through frequency conversion.[22] While numerous oxide-based NLO materials are already available in the market for applications near the visible range, there is demand for the development of novel NLO materials working at IR wavelengths. Chalcogenides can efficiently generate conversion wavelengths in the near- and mid-IR via phase matching and are broadly transparent in the IR due to their low-energy stretching frequencies.[23−25] Current industry-standard IR materials include $AgGaS_2$, $AgGaSe_2$, and $ZnGeP_2$, which have good SHG coefficients (d_{36} ∼ 23−70 pm/V and λ = 0.5−12.5 μm)[26] and can be grown as large single crystals via the Bridgman−Stockbarger method.[27,28] However, their practical use, especially under high-intensity incident beams, is limited by their low laser-induced damage thresholds (LIDTs). New wide gap IR NLO materials must be discovered which have superior LIDTs compared with the current benchmark materials.

Higher harmonic generation via chalcogenides is largely done by designing devices, such as by using phase-change materials or metasurfaces,[29−31] while absolute THG measurements are compared against SHG reference materials such as $AgGaS_2$ and $AgGaSe_2$.[16,32] Other material classes measure against transition metal dichalcogenides such as WS_2,[33] or α-quartz,[34,35] but there is a lack of appropriate reference materials for THG because the field has focused on materials optimization and engineering rather than materials discovery. This is particularly lamentable because all materials, regardless of their internal symmetry, have a THG response. Wide-gap chalcogenides such as $Li_4P_2S_6$ have great potential to act as high-power sources in the ultraviolet and visible ranges, but so little research has been done to understand the nature of THG in bulk materials that it is impossible to hypothesize which materials perform better than others. We have developed structure−property relationships for SHG after decades of materials discovery and careful optical and theoretical analyses, and we must similarly work toward understanding the nature of THG in bulk materials. More materials must be studied for their THG response so that we may begin building models, testing predictions, and establishing an intuitive understanding of THG and other important third-order NLO processes.

Herein, we report the first single-crystal diffraction experiment and the nonlinear response of $Li_4P_2S_6$, which confirm the noncentrosymmetric *P*321 space group reported by Neuberger et al.[5] There is positional disorder in each of the 3 P atoms, likely due to the 0-D nature of the material. The thermal behavior of the title compound was investigated up to 1000 °C. $Li_4P_2S_6$ is a wide-gap semiconductor (E_g = 3.74 eV) with good transparency in the IR (1.6−16.6 μm), and density functional theory calculations show that it is a nearly direct-gap material. At 1600 nm, $Li_4P_2S_6$ exhibits non-phase matchable SHG (∼0.1 × $AgGaSe_2$); however, the LIDT of $Li_4P_2S_6$ is much higher than that of $AgGaSe_2$ by a factor of ∼16. Additionally, $Li_4P_2S_6$ exceeds the THG (∼36×) of $AgGaSe_2$ in the near-IR due to self-absorption of the $AgGaSe_2$ reference at near-bandgap energies. Our results indicate that $Li_4P_2S_6$ has potential for high-power NLO applications at near- and mid-IR frequencies.

EXPERIMENTAL SECTION

Starting Materials. All manipulations were performed under a dry nitrogen atmosphere in a glove box. The commercially available chemicals bismuth (Bi, American Elements, 99.999%), lithium (Li, Sigma-Aldrich, 99.9%), phosphorous (P, Alfa Aesar, 99.999%), and sulfur (S, 5N Plus Inc., 99.99%) were used without further purification. Li_2S was prepared via the literature procedure by reacting the alkali metal and chalcogen in liquid ammonia.[14,36] P_2S_4 was prepared by grinding stoichiometric amounts of P (3.257 g, 0.105 mol) and S (6.743 g, 0.210 mol) in an agate mortar and pestle and charged to an aluminum-lined fused silica tube (13 mm OD and 11 mm ID). The aluminum was removed, and the fused silica tube was transferred to a vacuum line, evacuated to ∼3 × 10^{-3} mbar, flame sealed, and loaded into a programmable tube furnace. The reactants were heated to 550 °C over 10 h and held at 550 °C for 36 h, after which the furnace was turned off, and the tube was allowed to cool to room temperature before opening. The synthesis yielded a yellow polycrystalline ingot composed of a variety of P_xS_y binaries.

Synthesis of Polycrystalline $Li_4P_2S_6$. Stoichiometric amounts of Li_2S (0.326 g, 7.096 mmol) and P_2S_4 (0.674 g, 3.544 mmol) were ground together in a N_2-filled glovebox and charged to an aluminum-lined, triple carbon-coated fused silica tube (13 mm OD and 11 mm ID). The starting materials must be charged in a glovebox due to the air sensitivity of Li_2S. The aluminum was removed, the fused silica tube was transferred to a vacuum line, evacuated to ∼3 × 10^{-3} mbar, flame sealed, and loaded into a programmable tube furnace. The reactants were heated to 400 °C over 6 h and held at 400 °C for 18 h, after which the furnace was turned off, and the tube was allowed to cool to room temperature before opening. The synthesis yielded a phase-pure white powder. The tube was opened in the glovebox to prevent any reaction to the atmosphere. Synthesis of a larger-scale batch required an additional, identical heating profile to ensure all starting materials and intermediate phases fully reacted to the target material.

Synthesis of Single-Crystal $Li_4P_2S_6$. Single crystals of $Li_4P_2S_6$ were serendipitously found during an exploratory reaction targeting the stoichiometry $LiBiP_2S_6$. Stoichiometric amounts of Li_2S (0.0244 g, 0.531 mmol), Bi (0.222 g, 1.062 mmol), P_2S_5 (0.236 g, 1.062 mmol),

https://doi.org/10.1021/acs.chemmater.3c01783
Chem. Mater. 2023, 35, 7322−7332

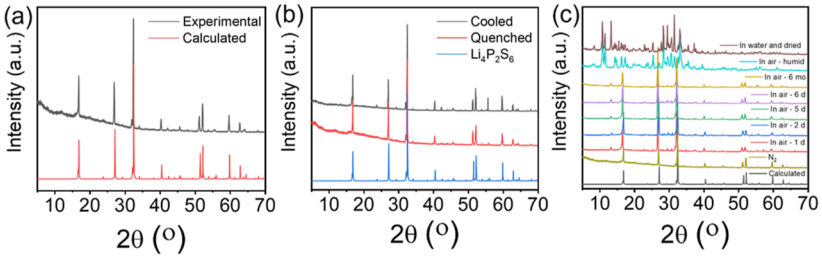

Figure 1. PXRD results showing (a) the purity of prepared material versus the calculated powder pattern and (b) a comparison of slow-cooled versus quenched materials. Both cooling profiles produced highly pure polycrystalline materials. (c) shows the air and moisture stability of the material. The laboratory had relatively stable low humidity (~30%), but at one point, it was sufficiently humid to fully hydrate the material. A powder pattern was also taken after mixing the material in water and drying it on a hot plate, resulting in a pattern which is very similar to the humidity-exposed material.

and S (0.017 g, 0.530 mmol) were ground together in a N_2-filled glovebox and charged to an aluminum-lined, triple carbon-coated fused silica tube (10 mm OD and 8 mm ID). The starting materials must be charged in a glovebox due to the air sensitivity of Li_2S. The aluminum was removed, the fused silica tube was transferred to a vacuum line, evacuated to ~3×10^{-3} mbar, flame sealed, and loaded into a programmable tube furnace. The reactants were heated to 500 °C over 10 h, held at 500 °C for 24 h, and cooled to room temperature over 24 h. Clear needles and hexagonal rods suitable for single-crystal X-ray diffraction (XRD) were optically identified and manually separated.

Single-Crystal X-ray Diffraction. Intensity data of the clear hexagonal rods of $Li_4P_2S_6$ was collected at 100 K. A suitable single crystal was mounted on a glass fiber with high vacuum grease on an XtaLAB Synergy diffractometer equipped with a micro-focus sealed X-ray tube, PhotonJet (Mo) X-ray, and a Hybrid Pixel (HyPix) array detector. The temperature of the crystal was controlled with an Oxford Cryosystems low-temperature device. Data reduction was performed with the CrysAlisPro software using an empirical absorption correction. The structure was solved with the ShelXT/SHELXS structure solution programs using intrinsic phasing/direct methods and by using Olex2 as the graphical interface. The model was refined with ShelXL using least-squares minimization. Data was collected at low temperatures and under a stream of N_2 to minimize hydration due to ambient conditions.

Powder SHG/THG/LIDT. Crystalline powders of $Li_4P_2S_6$ were provided for the SHG measurement: pristine and hydrated, where the latter was exposed to air for about a week. The samples were sieved with size ranges of <25, 25−53, 53−75, 75−106, 106−150, and >150 μm to examine the phase-matching behavior and LIDT of the samples. Each sample was sealed in a glass capillary tube and mounted on a homemade sample holder. The SHG efficiencies of the samples were compared with a reference material, $AgGaSe_2$.

The SHG measurements were carried out at room temperature using the input wavelength λ = 1600 nm and an intensity of 0.47 GW/cm^2. We confirmed that damage at this intensity is insignificant for both the sample and the reference. Coherent light with a wavelength of 1064 nm was initially produced using an EKSPLA PL-2250 series diode-pumped Nd:YAG laser with a pulse width of 30 ps and a repetition rate of 50 Hz to generate tunable pulses. The Nd:YAG laser pumped an EKSPLA harmonics unit (HU) H400, in which the input beam was frequency tripled by a cascade of NLO beam mixing. The 355 nm beam then entered an EKSPLA PG403-SH-DFG optical parametric oscillator (OPO) composed of four main parts: (i) a double-pass parametric generator, (ii) a single-pass parametric amplifier, (iii) a second-harmonic generator, and (iv) a difference-frequency generator. The wavelength from the OPO can be tuned from 210 to 4450 nm, and the output wavelength used in our SHG experiments was 1600 nm, which was deliberately selected to make sure that SHG (800 nm, i.e., 1.55 eV) occurred below the bandgap of both sample and reference. Therefore, the bandgap absorption of SHG can be neglected in the $\chi^{(2)}$ estimation. The SHG signal was collected using a collection lens system under a reflection geometry and guided by a fiber-optic bundle coupled to a high-resolution spectrometer (Horiba iHR320) equipped with a charge-coupled device camera (Horiba SYNAPSE). The data collection time was 20 s. The LIDTs of the sample and the reference were also assessed at λ = 1064 nm by monitoring the SHG response as a function of input intensity I_{input}.

Since both the reference ($AgGaSe_2$) and the sample ($Li_4P_2S_6$) exhibit non-phase-matchable SHG, THG must also be non-phase-matchable, and therefore, the smallest particle size yields the maximum THG. Therefore, THG measurements were carried out using the smallest particle size (<25 μm) of the reference and the pristine sample at room temperature at the input wavelengths λ = 1200, 1600, 2400, 2500, and 2600 nm. Here, the wavelength dependence was investigated for the practical THG efficiency as a function of λ in the IR. The THG signal was collected using the same collection lens system as for SHG and LIDT.

RESULTS AND DISCUSSION

Synthesis. We report a novel pathway for the synthesis of $Li_4P_2S_6$. Previous reports describe synthesis via the devitrification of glassy $Li_4P_2S_7$, in which 2 equiv of Li_2S and 1 equiv of P_2S_5 are combined stoichiometrically and then thermally decomposed to yield $Li_4P_2S_6$ and S,[3] or via the combination of 2 equiv of Li_2S, 2 equiv of P, and 4 equiv of S to yield the target compound.[3,5] Here, we synthesized the binary P_2S_4 to eliminate the extra step of devitrification to yield the target compound. Figure 1a shows powder-XRD of the title compound, showing the synthesis of pure material via the reaction profile described above. Furthermore, we found that the cooling speed did not affect the quality of the material, with air-quenched material yielding a similar purity to furnace-cooled material (Figure 1b). We additionally varied the amounts of the starting materials by adding up to one extra equivalent of both Li_2S and P_2S_4, and we find that our product is fairly tolerant of excess reagent. Figure S1a shows the effect of additional equivalents of Li_2S, and we see that up to a 0.5 molar excess of Li_2S presents almost negligible impurity peaks in the powder diffraction pattern. At one molar excess, the impurity peaks become as intense as the target peaks, with Li_3PS_4 and P_xS_y as the primary impurities. Adding additional equivalents of P_2S_4 yielded low-intensity impurity peaks of P_4S_9 and other P_xS_y binaries for up to 1 M excess P_2S_4 (Figure S1b). Figure 1c shows the air stability of the title compound over the course of several months. The laboratory maintains relatively low humidity (~30%), as shown by the minimal degradation of the material over 6 months in ambient conditions. There are slight hydration peaks at ~13° 2θ as well as between 26 and 32° 2θ which do not grow in intensity over the course of 6 months. We were unable to crystallographically assign the

https://doi.org/10.1021/acs.chemmater.3c01783
Chem. Mater. 2023, 35, 7322−7332

hydration peaks due to the hygroscopicity of the crystalline material. On a particularly humid day, there was severe degradation of the material which we identified through diffraction to be similar to a material obtained by mixing $Li_4P_2S_6$ with water and drying on a hot plate.

We also found that the reaction tube tended to rupture upon opening, indicating the production of gas as a byproduct, particularly when replicating reported syntheses at 900 °C. Tubes would often shatter and spread broken quartz inside the glovebox, so precautions must be taken when synthesizing $Li_4P_2S_6$. To limit this, the synthesis was carried out at several temperatures ranging from 350 to 500 °C to find a reaction temperature at which we could safely open the vessel. Figure S1c shows that the reaction fully proceeded at all tested temperatures, but lower temperatures tended to cause the vessel to burst less violently. In this vein, we attempted an exploratory reaction targeting $Li_4P_2Se_6$ with reaction conditions similar to those described here. We found the orange material to fume immediately upon contact with the atmosphere and burned through the weighing paper it was placed upon (Figure S2), in sharp contrast to the far more stable behavior of $Li_4P_2S_6$. Because NLO crystals should ideally be air-stable for applications, no further studies were conducted.

Crystallography. $Li_4P_2S_6$ crystallizes in the chiral $P321$ space group, as reported by Neuberger et al. in 2018.[5] The idealized structure they reported (Figure 2a) consists of

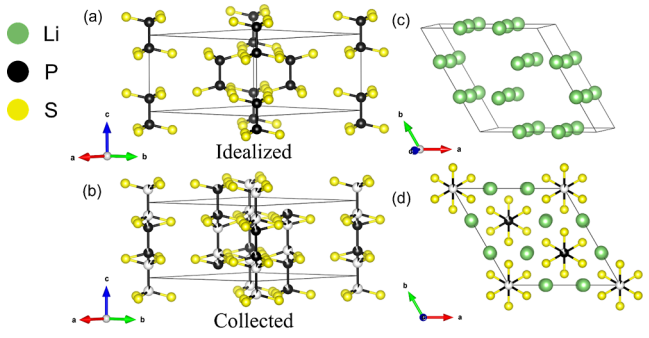

Figure 2. Single-crystal structure refinements comparing the ideal $Li_4P_2S_6$ structure reported by Neuberger[5] shown in (a) versus the refinement determined in this work shown in (b). The structures are comparable, and the main difference arises from the positional disorder of the three phosphorous sites. (c) shows the alignment of Li atoms through the unit cell. These Li sites are the source of noncentrosymmetry in the material, evident by the slight misalignment of Li atoms down the c-axis. (d) highlights the trigonal symmetry of the unit cell, specifically the staggered ethane conformation of the $[P_2S_6]^{4-}$ units. Adapted with permission from ref 5. Copyright 2018, Royal Society of Chemistry.

molecular staggered ethane-like $[P_2S_6]^{4-}$ units in an ABAB stacking pattern with a charge-balancing hexagonal net of Li^+. We similarly report a space group of $P321$; however, the molecular $[P_2S_6]^{4-}$ units show considerable disorder compared to the Neuberger structure (Figure 2b). Compared to 3 fully occupied P atoms, we similarly report 3 different phosphorous sites in the unit cell; however, each site is split crystallographically (Table 1). P1/P2 have an occupancy ratio of 93%/7%, respectively, while P3/P4 and P5/P6 both have occupancy ratios of 85%/15%, respectively. The Li net has no crystallographic splitting, and there are only subtle differences between the Li−Li−Li atomic angles reported here and from Neuberger (177.8 and 175.6° in Neuberger vs 175.1 and 175.9° reported here). Our examination of the P/S network shows that it hosts inversion, so the noncentrosymmetry originates in the Li net with very subtle off-centering of the Li atoms down the c-axis (Figure 2c), with Li−Li−Li atomic angles of 175.1° (Li1−Li3−Li1) and 175.9° (Li2−Li4−Li2). Furthermore, the crystal refinement shows near racemic twinning, with a twin law of $[-1, 0, 0; 0, 1, 1; 0, 0, -1]$ and a twin scale factor (BASF) of 0.508(5).

The refinement of this structure was not trivial because of multiple plausible structural solutions. There is precedence for this, as the original report in 1982 determined a space group of $P6_3/mcm$.[3] In Mercier et al.'s work, they were unable to resolve the individual P_2S_6 units and instead reported a 1-D chain of staggered ethane-like P_2S_6 units with only one P atomic position with 50% occupancy. Similarly, their Li net consisted of one independent position which forms columns of aligned Li atoms down the c-axis (Figure S3f). We found two additional structural solutions, which according to refinement statistics are high-quality solutions, both with R_1 values under 5% (Table S1). The alternate solutions have space groups $P\bar{3}m1$ and $P6_3mc$, with each solution showing significant occupational disorder. Each solution has 3 P sites: the $P\bar{3}m1$ solution suggests one fully occupied P atom and two P atoms with 75%/25% split occupancies; the $P6_3mc$ solution suggests one fully occupied P atom, one P atom split with an 89%/11% occupancy ratio, and one P atom with a 45%/55% occupancy ratio. There are additionally slight differences in the Li nets in each solution. The $P\bar{3}m1$ Li net has a hexagonal ordering similar to the $P321$ solution, but the Li−Li−Li atomic angle down the c-axis shows much less off-centering, with a near-ideal angle of 179.7°. $P\bar{3}m1$ is a centrosymmetric space group, so it was disqualified due to the presence of the SHG response in $Li_4P_2S_6$. The Li net of the $P6_3mc$ solution does not have three Li layers in the unit cell like the other solutions, but rather two distinct hexagonal moieties related via a 6_3 screw axis (Figure S3j). The $P6_3mc$ space group is acentric, but an analysis of the Ewald sphere shows forbidden reflections in the $0kl$ plane. The $P6_3mc$ space group has reflection conditions of $hh(-2h)l$: $l = 2n$ and $000l$: $l = 2n$, and Figure S4 shows clear reflection intensity at the (003), (00$\bar{3}$), and (00$\bar{5}$) indices, violating the $000l$: $l = 2n$ condition.

The quality of the crystal likely led to the multiple plausible refinements. The $Li_4P_2S_6$ structure solely consists of ethane-like $[P_2S_6]^{4-}$ units and charge-balancing Li^+ atoms. Other than P−S bonds, there are no covalent bonds to direct crystallization of the material, resulting in the highly disordered nature of the presented solution. To address this, equal atomic displacement parameter (EADP) constraints were required to give the P atoms equivalent thermal parameters, which helped the software find a converging solution.

Thermal Behavior. Differential thermal analysis (DTA) was performed on $Li_4P_2S_6$ in a vacuum-sealed, carbon-coated quartz ampule (Figure S5). There was one endothermic event upon heating at 625 °C and one exothermic event upon cooling (474 °C during the first heating cycle and 502 °C during the second heating cycle). There was no discernible crystallographic change in the material after the DTA experiment (Figure 3b), and the thermal events are not due to melting or re-crystallization as the material remained a fine powder after the heating cycles. In order to identify the origin of the thermal events, variable-temperature powder XRD (VT-PXRD) was performed on $Li_4P_2S_6$ sieved to a particle size

https://doi.org/10.1021/acs.chemmater.3c01783
Chem. Mater. 2023, 35, 7322−7332

Table 1. Structural Comparison of Previously and Currently Reported $Li_4P_2S_6$ Structure Solutions

structural features	$6_3/mcm$ (Mercier)	$P321$ (Neuberger)	$P321$ (this work)	$P\bar{3}m1$ (this work)	$P6_3mc$ (this work)
no. of Li sites	1	4	4	2	1
Li−Li−Li angle	180°	Li1−Li2−Li1: 177.8° Li3−Li4−Li3: 175.6°	Li1−Li3−Li1: 175.1° Li4−Li2−Li4: 175.9°	Li2−Li1−Li2: 179.5°	179.7°[a]
no. of P sites	1 (all 50% occupied)	3	3 (all split)	3 (2 split)	3 (2 split)
			P1: 93%/7%	P1: 75%/25%	P1: full occ.
			P2: 85%/15%	P2: 75%/25%	P2: 89%/11%
			P3: 85%/15%	P3: full occ.	P3: 55%/45%
no. of S sites	1	3	3	3	3

[a]Measured through 2 unit cells.

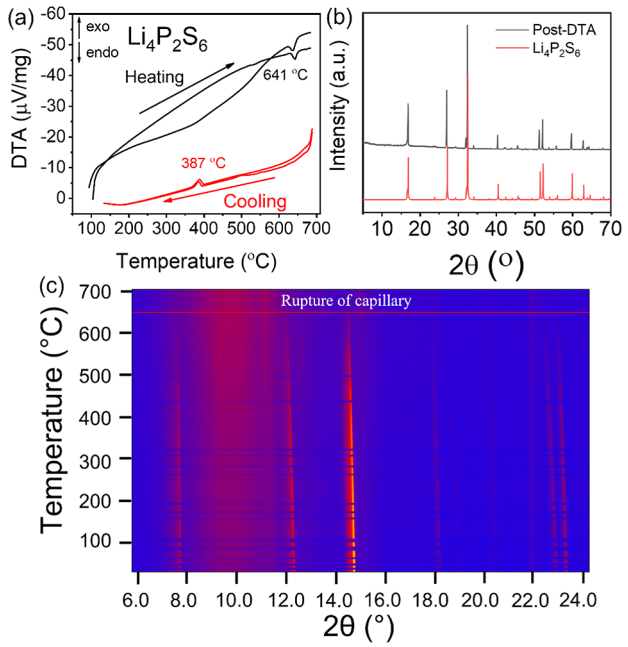

Figure 3. (a) shows the thermal behavior of $Li_4P_2S_6$ up to 700 °C heated at 10 °C/min in an alumina crucible in air under a stream of He gas. There is one thermal event upon heating at 641 °C and one thermal event upon cooling at 387 °C. (b) shows XRD patterns demonstrating that there is no crystallographic change in $Li_4P_2S_6$ before and after a DTA experiment performed in a vacuumized, carbon-coated, quartz ampule, while (c) shows the results of a failed VT-PXRD experiment in which a 0.7 mm diameter carbon-coated quartz capillary ruptured upon heating to approximately 650 °C, near the thermal event measured in (a). The intensity scales from blue to red, and the blue gaps in the thermal data are due to a lack of signal during the cooling regime.

below 50 μm. Figure 3c shows the results of the VT-PXRD experiment. The sample undergoes thermal expansion from room temperature to 650 °C, after which no more signal was detected from the sample. The capillary was found to have ruptured near 650 °C, corresponding to the thermal event measured upon heating the sample. This could be due to Li reaction with the quartz capillary or due to high gas pressures rupturing the 0.01 mm walls of the capillary.

To further investigate the origin of the thermal event, another DTA experiment was performed in conjunction with thermogravimetric analysis (TGA) and gas chromatography mass spectrometry (GC−MS). These probes allow us to identify the nature of the gases seen during synthesis and other experiments, the temperatures at which they evolve, and if any sample degradation was occurring. Figure 3a shows the DTA results when performed in an open container under a He stream. This time, there is no separation of the thermal events upon cooling. They are now at a lower temperature (387 °C), while the thermal event upon heating has risen to a slightly higher temperature (641 °C). Figure 4a shows the thermogram (TG) of the material in red, which corresponds to the heating profile shown in black. The heating profile was chosen to replicate the DTA experiments performed, followed by heating to 1000 °C to investigate the behavior under extreme conditions. There is considerable mass loss during the first heating cycle through the isothermal period at 700 °C. The corresponding GC−MS results are shown in Figure 4b−e. The first gaseous species detected is S_2 (m/z = 64) at minute 10.5, corresponding to a temperature of ∼95 °C. This is followed by simultaneous detection of H_2S, S_2, and S_3 (m/z = 34, 64, and 48, respectively) from minutes 25−30, corresponding to a temperature of ∼200 °C. The S_2 and S_3 peaks grow in intensity from minutes 30−60, drop significantly during the isotherm at 700 °C, regain their intensity during the cooling cycle, and stop at minute 108, corresponding to a temperature of ∼400 °C, roughly correlating to the boiling point of S at 444 °C.

At minute 60.5 (corresponding to a temperature of 568 °C), a new peak with m/z = 192 is detected. This has been assigned to $H_2P_2S_4$, with the H likely originating from atmospheric interactions during the course of the experiment.[37] $H_2P_2S_4$ was only detected from minutes 60−75: during heating and the isotherm at the maximum temperature of the experiment at 693 °C. During the second heating cycle, $H_2P_2S_4$ was not detected, but the S_2 and S_3 traces showed characteristics of the first heating cycle with reduced intensity. Furthermore, the second heating cycle showed much more stable thermal behavior up to the isotherm, likely because any volatile species had already off-gassed during the first heating cycle. The mass loss detected was only during the isothermal period (691 °C) and was relatively small compared to that during the first heating cycle. GC−MS data was only collected during the first 240 min of the experiment, but the DTA/TGA experiment was continued for an additional heating cycle to 1000 °C. Here, we see the most significant mass loss, leading to total decomposition/sublimation of the material. None was recovered to do a follow-up PXRD experiment. The mass loss onset was near minute 317, corresponding to a temperature of ∼540 °C, near the temperature at which $H_2P_2S_4$ was first detected. Mass loss was rapid through heating to 1000 °C, likely due to the continued evolution of $H_2P_2S_4$.

Electronic Structure and Spectroscopy. $Li_4P_2S_6$ is a wide gap semiconductor with a bandgap of 3.74 eV. As the material hydrates upon exposure to air, the primary absorption feature slightly shifts to lower energies (Figure 5a), resulting in

https://doi.org/10.1021/acs.chemmater.3c01783
Chem. Mater. 2023, 35, 7322−7332

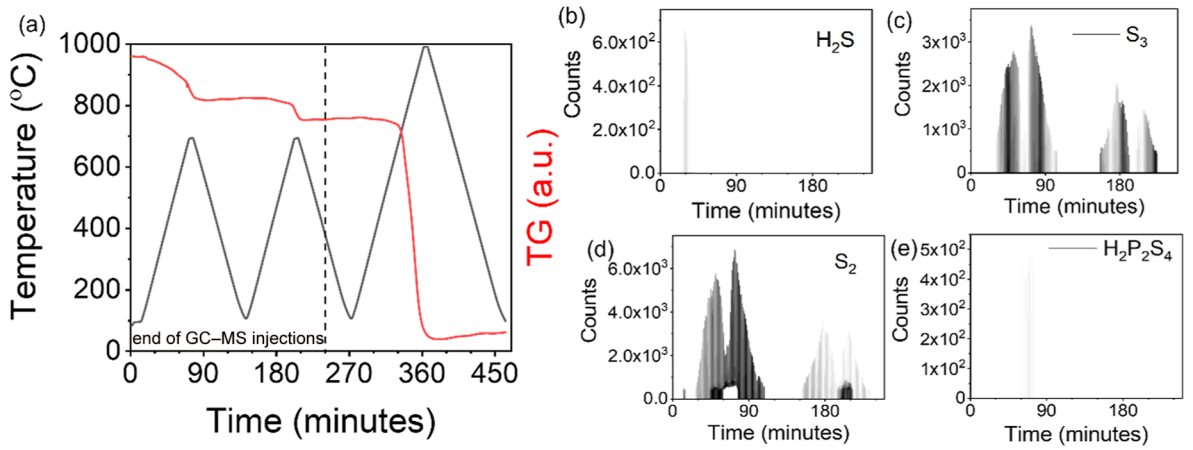

Figure 4. (a) shows a TG of $Li_4P_2S_6$ in red when heated in an open container under a stream of He from 100 to 1000 °C according to the heating profile in black. $Li_4P_2S_6$ undergoes considerable mass loss when heated above 650 °C. Continued heating to 1000 °C leads to the total degradation of the material. (b–e) show mass spectra of the non-atmospheric gaseous species detected during the first 240 min of the heating profile in (a). (b) shows counts of H_2S (assigned to m/z = 34); (c) shows counts of S_3 (assigned to m/z = 48); (d) shows counts of S_2 (assigned to m/z = 64); and (e) shows counts of $H_2P_2S_4$ (assigned to m/z = 192).

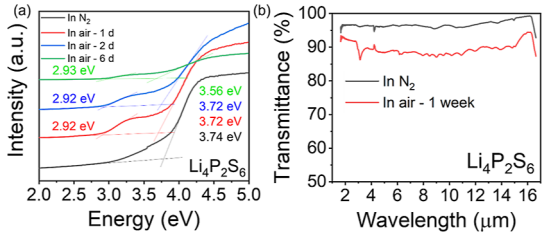

Figure 5. (a) shows diffuse reflectance measurements taken over the course of 6 days. The main absorption event at 3.74 eV persists as the material hydrates, while a secondary event grows in at 2.92 eV, likely due to the hydration of the material. (b) shows FTIR measurements of the pristine and hydrated materials. The overall transmittance remains high, while a peak at approximately 3 μm grows in after a week exposed to the atmosphere, corresponding to O–H stretches in water.

a decreased bandgap of 3.56 eV. In addition to this redshift, there is a secondary absorption feature which increases over the course of hydration. This additional absorption peak is centered at 2.92 eV and is likely due to the formation of a hydrated phase. This is corroborated by Fourier transform infrared spectroscopy (FTIR), as shown in Figure 5b. FTIR data was taken on pristine material from a N_2-filled glovebox and is compared against material which was exposed to ambient conditions for 1 week. The overall transmittance (% T) of the pristine material is approximately 97%, while the transmittance of the hydrated material falls to approximately 87%. In addition, there is an additional feature at 3 μm, corresponding to the O–H stretch of water. Despite some degradation in the material due to hydration, $Li_4P_2S_6$ remains highly transparent across the entire infrared region, showing promise for NLO applications in ambient conditions.

Theoretical calculations show that $Li_4P_2S_6$ has an indirect bandgap (Figure 6a) with the valence band maximum at Γ and the conduction band minimum very slightly shifted toward the A point in the Brillouin zone. The valence bands of $Li_4P_2S_6$ are degenerate and relatively flat, likely due to the 0-D nature of the material.[13] An analysis of the density of states (DOS) shows that the valence band from approximately −3 to 0 eV is dominated by the sulfur s- and p-states, with negligible contributions from both the Li and P atoms. The conduction band has approximately equal contributions from the S and P s- and p-states and negligible contributions from the Li atoms. The highly localized nature of the electron density in the valence band stems from the ionic nature of the $[P_2S_6]^{4-}$ units surrounded by Li^+ atoms. Figure S6 shows the calculated electron localization function (ELF) for $Li_4P_2S_6$. The ELF plots present different slices of the electron density moving along the c-axis of the unit cell (Figure S6d). Figure S6a shows the highly concentrated electron density of the Li^+ ions, while Figure S6b,c shows more delocalized electron densities on the P and S atoms, respectively. The electron density of the unit cell is largely restricted to the $[P_2S_6]^{4-}$ units due to their

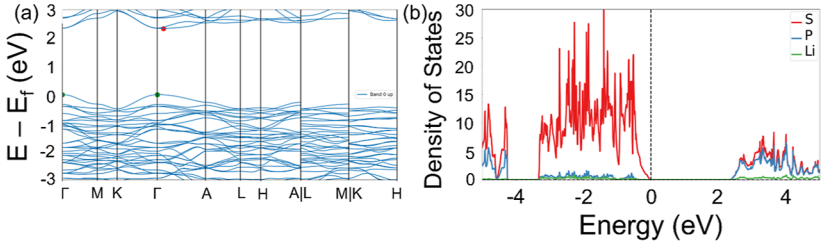

Figure 6. Theoretical calculations of the band structure and DOS of $Li_4P_2S_6$. (a) shows the band structure of $Li_4P_2S_6$, which has a nearly direct bandgap centered near the Γ point. The valence band maximum occurs at Γ (green-filled circle), while the conduction band minimum (red-filled circle) is slightly shifted from Γ toward A. (b) shows that the valence band is almost entirely composed of S states, while the conduction band shows a relatively equal contribution from both S and P states.

https://doi.org/10.1021/acs.chemmater.3c01783
Chem. Mater. 2023, 35, 7322–7332

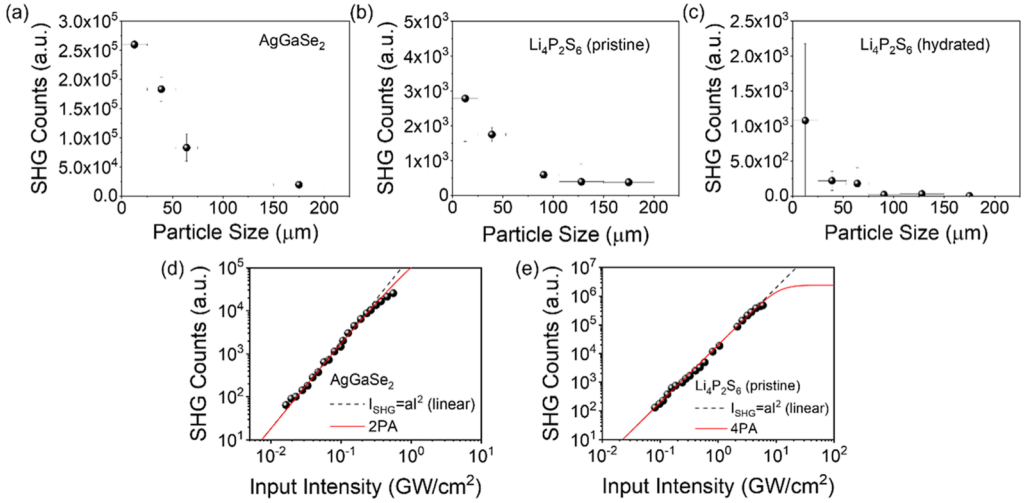

Figure 7. (a–c) show SHG output as a function of particle size for (a) $AgGaSe_2$, (b) pristine $Li_4P_2S_6$, and (c) hydrated $Li_4P_2S_6$. All samples are non-phase-matchable. Pristine $Li_4P_2S_6$ underperforms the SHG of $AgGaSe_2$ by a factor of approximately 10, while the hydrated sample gives approximately 60% of the output of the pristine material. (d,e) show the LIDT results from $AgGaSe_2$ and pristine $Li_4P_2S_6$, respectively. $Li_4P_2S_6$ has a greatly improved LIDT (15.8 × $AgGaSe_2$) due to its wide bandgap.

covalency, while the ionic nature of the Li^+ atoms keeps intermolecular interactions to a minimum.

SHG/LIDT Studies. Figure 7a–c plot the size-dependent SHG counts measured from the reference, $Li_4P_2S_6$ (pristine), and $Li_4P_2S_6$ (hydrated) at λ = 1600 nm, respectively. The existence of the SHG signal from $Li_4P_2S_6$ confirms the noncentrosymmetric structure of the crystal.[19] Both the pristine and hydrated samples are non-phase-matchable at this wavelength, which means that the SHG intensity decreases as the particle size increases. This is the reason $AgGaSe_2$ was chosen as the reference material since it is also not phase-matchable at λ = 1600 nm. Although $AgGaSe_2$ could not be measured for 75–106 μm and 106–150 μm, it has been reported that the SHG intensity of $AgGaSe_2$ decreases monotonically at λ = 1600 nm, indicating that its coherence length is smaller than 25 μm.[38] Large standard deviations in the SHG counts for <25 μm in both samples are related to rather inhomogeneous size distributions of the powders. The measurements for this size were performed at 8 different excitation positions and at 13 different excitation positions for the pristine and hydrated samples, respectively.

Using the Kurtz powder method, the second-order susceptibility of each sample, $\chi_S^{(2)}$, was calculated for the non-phase-matching case[39,40]

$$\chi_S^{(2)} = \chi_R^{(2)} \frac{l_R}{l_S} \left(\frac{I_S^{SHG}}{I_R^{SHG}} \right)^{1/2} \tag{1}$$

where $\chi_R^{(2)}$ is the second-order susceptibility of the reference, l_S and l_R are the experimental SHG coherence lengths of the sample and the reference, and I_S^{SHG} and I_R^{SHG} are the measured maximum SHG counts from the sample and the reference, respectively. However, the experimental coherence lengths are all smaller than 25 μm, which means that the exact coherence lengths cannot be determined experimentally. Thus, we assumed that l_R/l_S = 1, where the coherence lengths of the reference and the samples are approximately equal. Note that this assumption could overestimate or underestimate $\chi_S^{(2)}$.

The effective SHG coefficient, $d_{eff} = \chi_{eff}^{(2)}/2$, of the reference material was calculated to be 28 pm/V according to the Kurtz powder method[39]

$$\langle (d_{eff})^2 \rangle = \frac{19}{105} \sum_i (d_{iii}^{2\omega})^2 + \frac{13}{105} \sum_{i \neq j} d_{iii}^{2\omega} d_{ijj}^{2\omega} + \frac{44}{105} \sum_{i \neq j} (d_{iij}^{2\omega})^2 + \frac{13}{105} \sum_{ijk,\text{cyclic}} d_{iij}^{2\omega} d_{jkk}^{2\omega} + \frac{5}{7} (d_{ijk}^{2\omega})^2 \tag{2}$$

where the nonzero d_{ij} tensor elements for $AgGaSe_2$ ($\bar{4}2m$) are $d_{36} = d_{25} = d_{14} = 33$ pm/V in the contracted susceptibility tensor notation[19,41]

$$d_{ij}(AgGaSe_2) = \begin{pmatrix} 0 & 0 & 033 & 0 & 0 \\ 0 & 0 & 00 & 33 & 0 \\ 0 & 0 & 00 & 0 & 33 \end{pmatrix} \tag{3}$$

Using $\chi_{R,eff}^{(2)}$ = 56 pm/V,[38] our calculation yields $\chi_{S,eff}^{(2)}$(pristine) ~ 5.8 ± 1.3 pm/V and $\chi_{S,eff}^{(2)}$(hydrated) ~ 3.6 ± 1.8 pm/V at λ = 1600 nm (Table 2). These values rival those of highly polarizable heavy metal-containing materials, even though the most polarizable atom in this material is S. Due to the highly racemic (50.8%/49.2%) nature of the material, the powder SHG measurement likely severely underestimates the intrinsic SHG output of a single enantiomer.

Table 2. SHG and LIDT Comparison of $AgGaSe_2$ and Pristine/Hydrated $Li_4P_2S_6$

	$AgGaSe_2$	$Li_4P_2S_6$ (pristine)	$Li_4P_2S_6$ (hydrated)
$\chi_{eff}^{(2)}$ (pm/V) (1600 nm)	56	5.8 ± 1.3	3.6 ± 1.8
LIDT (GW/cm^2) (1064 nm)	0.24	3.8	N/A
β (cm/GW) (1064 nm)	90	N/A	N/A
δ (cm^5/GW^3) (1064 nm)	N/A	0.061	N/A

https://doi.org/10.1021/acs.chemmater.3c01783
Chem. Mater. 2023, 35, 7322–7332

To assess the LIDT, the SHG counts for the reference and the pristine sample at d = 25−53 μm were measured as a function of input intensity at 1064 nm (Figure 7d,e). The measured SHG coefficient for the hydrated sample is not an intrinsic value, and therefore, the LIDT was not assessed. $AgGaSe_2$ is two-photon absorption (2 PA) active at this excitation wavelength. However, in the case of $Li_4P_2S_6$ (pristine), the bandgap (3.74 eV) is much larger than twice the photon energy corresponding to 1064 nm. In fact, the pristine sample is four-photon absorption (4 PA) active at λ = 1064 nm. The SHG counts are proportional to the SHG intensity, I_{SHG}, which is given by

$$I_{SHG} = aI_{input}^2 \tag{4}$$

where a is a proportionality constant that incorporates $\chi^{(2)}$ and I_{input} is the fundamental input intensity. We found that the fundamental light starts to undergo depletion due to 2 PA and 4 PA with increasing I_{input}, as evidenced by the gradual deviation from the dashed line (eq 4) in each plot of Figure 7d ($AgGaSe_2$) and Figure 7e ($Li_4P_2S_6$). The effect of 2 PA and 4 PA can be incorporated by

$$I_{SHG,2PA} = aI_{2PA}^2 \text{ with } I_{2PA} = \frac{I_{input}}{1 + \beta d I_{input}} \tag{5}$$

$$I_{SHG,4PA} = aI_{4PA}^2 \text{ with } I_{4PA} = \frac{I_{input}}{(1 + 3\delta d I_{input}^3)^{1/3}} \tag{6}$$

where I_{2PA} and I_{4PA} are the modified input intensities by 2 PA and 4 PA, which are derived from the nonlinear Beer−Lambert law,[42−44] respectively. In eqs 5 and 6, d is the particle size, β is the 2 PA coefficient, and δ is the 4 PA coefficient. The fitted values of β and δ are approximately 90 cm/GW and 0.061 cm^5/GW^3 for $AgGaSe_2$ and $Li_4P_2S_6$, respectively. We estimated the LIDT as the intensity at which the SHG counts (black dots) deviate from the black dashed line in Figure 7d,e. Accordingly, the LIDTs of $AgGaSe_2$ and $Li_4P_2S_6$ (pristine) are 0.24 GW/cm^2 and 3.8 GW/cm^2, respectively.

THG Study. First, we measured the THG responses at λ = 2400−2600 nm, where the corresponding THG photon energy (1.43−1.55 eV; 867−800 nm in wavelength) is well below the bandgap for both the reference (1.8 eV)[45] and the sample (3.74 eV). This condition must be established for the estimation of the THG coefficient (third-order nonlinear susceptibility) without any complication arising from bandgap absorption of THG. Since the THG coherence length cannot be experimentally determined, the third-order nonlinear susceptibility, $\chi^{(3)}$, was calculated using the Kurtz powder method for the non-phase-matching case[16]

$$\chi_S^{(3)} = \chi_R^{(3)} \left(\frac{I_S^{THG}}{I_R^{THG}} \right)^{1/2} \tag{7}$$

where $\chi_S^{(3)}$ and $\chi_R^{(3)}$ are the third-harmonic coefficients for the sample and reference and I_S^{THG} and I_R^{THG} are the measured THG counts from the sample and the reference, respectively. Table S14 shows the intensity in counts of THG generation for the sample and the reference as a function of wavelength, and Table 3 lists the $\chi_S^{(3)}$ values at the three wavelengths calculated using $\chi_R^{(3)}$ = 1.60 × 10^5 pm^2/V^2 for $AgGaSe_2$,[16] indicating a case for a near-static limit with an insignificant λ dependence. Between 2400 and 2600 nm, $Li_4P_2S_6$ has an effective $\chi^{(3)}$ of ~0.34 × 10^5 pm^2/V^2. Friedrich et al. measured powder THG of the family $AGaMQ_4$ (A = K, Rb, Cs, Tl; M = Ge, Sn; and Q = S, Se) at an incident wavelength of 1800 and 2400 nm, yielding a $\chi^{(3)}$ range of 0.34−2.26 × 10^5 pm^2/V^2. From this family, $Li_4P_2S_6$ has a comparable $\chi^{(3)}$ coefficient to $KGaGeS_4$, $CsGaGeS_4$, $CsGaSnS_4$, and $CsGaSnSe_4$, materials which are layered and contain highly polarizable elements such as Sn and Se.[16] In order to compare with the reference, the ratio of $\chi^{(3)}$ values between the sample and the reference is listed in Table 3. It is interesting to note that this relative $\chi^{(3)}$ value of ~0.2 is about twice as large than that for $\chi^{(2)}$, ~0.1 as determined from the SHG measurement, indicating that the title compound has a good potential for $\chi^{(3)}$ properties that do not require any phase-matching requirement for practical applications.[46]

Table 3. $\chi^{(3)}$ of $Li_4P_2S_6$ and $\chi_S^{(3)}/\chi_R^{(3)}$ at λ_{THG} = 800, 833, and 867 nm

THG wavelength (nm)	800	833	867
$\chi_S^{(3)}$ (×10^5 pm^2/V^2)	0.309 ± 0.034	0.359 ± 0.049	0.381 ± 0.044
$\chi^{(3)}$ ratio	0.194 ± 0.021	0.224 ± 0.031	0.239 ± 0.028

Inspired by this, we measured the THG at shorter wavelengths such as 1200 and 1600 nm because the THG of the reference would be severely depleted due to bandgap absorption, while $Li_4P_2S_6$ has a sufficiently large bandgap to not be similarly inhibited. Figure 8 shows the THG output of the sample and reference at 1200 nm (Figure 8a) and 1600 nm (Figure 8b), as well as a comparison across all wavelengths measured (Figure 8c). $Li_4P_2S_6$ becomes much more efficient at shorter wavelengths compared with the reference. In fact, $AgGaSe_2$ barely exhibits THG at 1200 nm, as indicated by the red trace in Figure 8a, in which the THG signal at 400 nm is almost completely absorbed. At 1600 nm, which is near the telecommunication wavelength, THG from $Li_4P_2S_6$ (blue trace) is about 6 times superior to $AgGaSe_2$ (red trace), as shown in Figure 8b.

We further argue that the title compound is an excellent $\chi^{(3)}$ material based upon a theoretical model that approximately relates $\chi^{(3)}$ and the bandgap energy. According to the two-band model,[47,48] the real part of $\chi^{(3)}$, n_2, is given by

$$n_2 = K \frac{\hbar c \sqrt{E_p}}{2 n_0^2 E^4} G_2(\hbar\omega/E) \tag{8}$$

where K is the Kane parameter, $\hbar$ is the Planck constant, c is the speed of light at vacuum, E_p is a material-independent constant, n_0 is the linear refractive index, E is the bandgap, G_2 is a function representing the frequency dependence of n_2, and ω is the angular frequency of the incident photon. The relation between $\chi^{(3)}$ and n_2 is[19]

$$n_2 = \frac{3}{4 n_0^2 \epsilon_0 c} \chi^{(3)} \tag{9}$$

Combining eqs 8 and 9, the bandgap dependence of $\chi^{(3)}$ is given by

$$\chi^{(3)} \propto \frac{G_2(\hbar\omega/E)}{E^4} \tag{10}$$

because both K and E_p can be considered nearly material-independent for direct-bandgap semiconductors.[48] Therefore, a theoretical prediction for the ratio of the THG coefficients can be represented by

https://doi.org/10.1021/acs.chemmater.3c01783
Chem. Mater. 2023, 35, 7322−7332

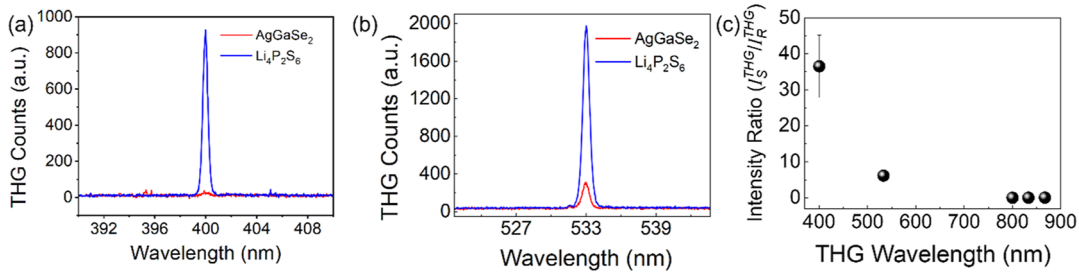

Figure 8. THG response as a function of wavelength for $Li_4P_2S_6$ vs $AgGaSe_2$. (a) shows the THG counts of the sample (blue) versus the reference (red) with a 1200 nm incident beam, (b) shows the THG counts of the sample (blue) versus the reference (red) with a 1600 nm incident beam, and (c) shows the relative output intensities between the sample and the reference in our experimental range.

$$\frac{\chi_S^{(3)}}{\chi_R^{(3)}} \approx \frac{G_2(\hbar\omega/E_S)}{G_2(\hbar\omega/E_R)}\left(\frac{E_R}{E_S}\right)^4 \tag{11}$$

where E_S = 3.74 eV and E_R = 1.8 eV are the bandgap energies of the sample and the reference, respectively. By considering the band dispersions for both sample and reference at the near-static regime via G_2, the calculated $\chi^{(3)}$ ratio is 0.040−0.042 over λ = 2400−2600 nm. Instead, the experimentally determined ratio in Table 3 is about 5 times larger than this theoretical prediction, further demonstrating that our material is an excellent THG material.

CONCLUSIONS

$Li_4P_2S_6$ crystallizes in the *P*321 space group, and it can be directly synthesized from binary compounds at temperatures as low as 350 °C, much lower than previously reported. $Li_4P_2S_6$ is thermally stable up to approximately 600 °C, after which it begins to thermally decompose and off-gas as a combination of S and P_2S_4. $Li_4P_2S_6$ has a wide, near-direct bandgap of 3.74 eV. The SHG response of near-racemic $Li_4P_2S_6$ is moderate (~0.1 × $AgGaSe_2$) but its LIDT is exceptional (~15.8 × $AgGaSe_2$), which follows the well-established trend of SHG being inversely proportional to the bandgap and LIDT being proportional to the bandgap.[7] The wide bandgap of the material enables strong THG at much lower wavelengths than the reference due to a lack of bandgap absorption, and we see THG intensities up to 36× the reference at 1200 nm and 6× the reference at 1600 nm, which is important for applications such as telecommunications.

ASSOCIATED CONTENT

Supporting Information

The Supporting Information is available free of charge at https://pubs.acs.org/doi/10.1021/acs.chemmater.3c01783.

Experimental methods and physical property measurements; X-ray crystallographic data tables of atomic coordinates, anisotropic displacement parameters, bond lengths, and grouped bond angles for $Li_4P_2S_6$ in the *P*321, $P\bar{3}m1$, and $P6_3mc$ space groups; THG intensity data; PXRD showing experimental results from varying reagent ratios; pyrophoric behavior of $Li_4P_2Se_6$; visual comparison between reported and published space groups of $Li_4P_2S_6$; reflection condition violations for the $P6_3mc$ solution; DTA performed under vacuum; ELF calculation results; and mass spectra of atmospheric gases (PDF)

Accession Codes

CSD number for $Li_4P_2S_6$: 2268309.

AUTHOR INFORMATION

Corresponding Authors

Joon I. Jang − *Department of Physics, Sogang University, Seoul 04107, South Korea;* orcid.org/0000-0002-1608-8321; Email: jjcoupling@sogang.ac.kr

Mercouri G. Kanatzidis − *Department of Chemistry, Northwestern University, Evanston, Illinois 60208, United States; Materials Science Division, Argonne National Laboratory, Argonne, Illinois 60439, United States;* orcid.org/0000-0003-2037-4168; Email: m-kanatzidis@northwestern.edu

Authors

Benjamin M. Oxley − *Department of Chemistry, Northwestern University, Evanston, Illinois 60208, United States; Materials Science Division, Argonne National Laboratory, Argonne, Illinois 60439, United States;* orcid.org/0000-0003-1571-1924

Kyeong-Hyeon Lee − *Department of Physics, Sogang University, Seoul 04107, South Korea*

Thomas S. Ie − *Department of Chemistry, Northwestern University, Evanston, Illinois 60208, United States; Materials Science Division, Argonne National Laboratory, Argonne, Illinois 60439, United States*

Jae Mo Lee − *Department of Physics, Sogang University, Seoul 04107, South Korea*

Michael J. Waters − *Department of Materials Science and Engineering, Northwestern University, Evanston, Illinois 60208, United States;* orcid.org/0000-0001-6425-4331

James M. Rondinelli − *Department of Materials Science and Engineering, Northwestern University, Evanston, Illinois 60208, United States;* orcid.org/0000-0003-0508-2175

Complete contact information is available at: https://pubs.acs.org/10.1021/acs.chemmater.3c01783

Notes

The authors declare no competing financial interest.

ACKNOWLEDGMENTS

We thank Charlotte Stern for her help with the crystal structure solution. M.G.K., B.M.O., and T.S.I. acknowledge the National Science Foundation Solid State and Materials Chemistry Division for their support (DMR-2305731). The IMSERC PCM facility at the Northwestern University used in this work received support from the Soft and Hybrid Nanotechnology Experimental (SHyNE) Resource (NSF ECCS-2025633) and Northwestern University. The computational work by J.M.R. and M.J.W. was supported by the National Science Foundation's MRSEC program (DMR-

1720139) at the Materials Research Center of Northwestern University. J.I.J. acknowledges the support of the Basic Science Research Program (2021R1A2C2013625) and the Basic Research Laboratory Program (2022R1A4A1033562) through the National Research Foundation of Korea (NRF), funded by the Korean government. This work made use of the IMSERC Crystallography facility at Northwestern University, which has received support from the Soft and Hybrid Nanotechnology Experimental (SHyNE) Resource (NSF ECCS-2025633), the State of Illinois, and Northwestern University.

REFERENCES

(1) Dietrich, C.; Sadowski, M.; Sicolo, S.; Weber, D. A.; Sedlmaier, S. J.; Weldert, K. S.; Indris, S.; Albe, K.; Janek, J.; Zeier, W. G. Local Structural Investigations, Defect Formation, and Ionic Conductivity of the Lithium Ionic Conductor $Li_4P_2S_6$. *Chem. Mater.* **2016**, *28*, 8764−8773.

(2) Minami, K.; Mizuno, F.; Hayashi, A.; Tatsumisago, M. Lithium ion conductivity of the Li_2S-P_2S_5 glass-based electrolytes prepared by the melt quenching method. *Solid State Ionics* **2007**, *178*, 837−841.

(3) Mercier, R.; Malugani, J. P.; Fahys, B.; Douglande, J.; Robert, G. Synthese, structure cristalline et analyse vibrationnelle de l'hexathiohypodiphosphate de lithium $Li_4P_2S_6$. *J. Solid State Chem.* **1982**, *43*, 151−162.

(4) Hood, Z. D.; Kates, C.; Kirkham, M.; Adhikari, S.; Liang, C.; Holzwarth, N. A. W. Structural and electrolyte properties of $Li_4P_2S_6$. *Solid State Ionics* **2016**, *284*, 61−70.

(5) Neuberger, S.; Culver, S. P.; Eckert, H.; Zeier, W.; Schmedt auf der Günne, J. Refinement of the crystal structure of $Li_4P_2S_6$ using NMR crystallography. *Dalton Trans.* **2018**, *47*, 11691−11695.

(6) Haynes, A. S.; Saouma, F. O.; Otieno, C. O.; Clark, D. J.; Shoemaker, D. P.; Jang, J. I.; Kanatzidis, M. G. Phase-Change Behavior and Nonlinear Optical Second and Third Harmonic Generation of the One-Dimensional $K_{(1-x)}Cs_xPSe_6$ and Metastable β-$CsPSe_6$. *Chem. Mater.* **2015**, *27*, 1837−1846.

(7) Saouma, F. O.; Stoumpos, C. C.; Wong, J.; Kanatzidis, M. G.; Jang, J. I. Selective enhancement of optical nonlinearity in two-dimensional organic-inorganic lead iodide perovskites. *Nat. Commun.* **2017**, *8*, 742.

(8) Bera, T. K.; Jang, J. I.; Ketterson, J. B.; Kanatzidis, M. G. Strong Second Harmonic Generation from the Tantalum Thioarsenates $A_3Ta_2AsS_{11}$ (A = K, Rb). *J. Am. Chem. Soc.* **2009**, *131*, 75−77.

(9) He, J.; Iyer, A. K.; Waters, M. J.; Sarkar, S.; Zu, R.; Rondinelli, J. M.; Kanatzidis, M. G.; Gopalan, V. Giant Non-Resonant Infrared Second Order Nonlinearity in γ-$NaAsSe_2$. *Adv. Opt. Mater.* **2021**, *10*, 2101729.

(10) Iyer, A. K.; He, J.; Xie, H.; Goodling, D.; Chung, D.-Y.; Gopalan, V.; Kanatzidis, M. G. Stabilization of the Polar Structure and Giant Second-Order Nonlinear Response of Single Crystal γ-$NaAs_{0.95}Sb_{0.05}Se_2$. *Adv. Funct. Mater.* **2022**, *33*, 2211969.

(11) Oxley, B. M.; Cho, J. B.; Iyer, A. K.; Waters, M. J.; He, J.; Smith, N. C.; Wolverton, C.; Gopalan, V.; Rondinelli, J. M.; Jang, J. I.; Kanatzidis, M. G. Heteroanionic Control of Exemplary Second-Harmonic Generation and Phase Matchability in 1D $LiAsS_{2-x}Se_x$. *J. Am. Chem. Soc.* **2022**, *144*, 13903−13912.

(12) Iyer, A. K.; Cho, J. B.; Byun, H. R.; Waters, M. J.; Hao, S.; Oxley, B. M.; Gopalan, V.; Wolverton, C.; Rondinelli, J. M.; Jang, J. I.; Kanatzidis, M. G. Structure Tuning, Strong Second Harmonic Generation Response, and High Optical Stability of the Polar Semiconductors $Na_{1-x}K_xAsQ_2$. *J. Am. Chem. Soc.* **2021**, *143*, 18204−18215.

(13) Song, J.-H.; Freeman, A. J.; Bera, T. K.; Chung, I.; Kanatzidis, M. G. First-principles prediction of an enhanced optical second-harmonic susceptibility of low-dimensional alkali-metal chalcogenides. *Phys. Rev. B: Condens. Matter Mater. Phys.* **2009**, *79*, 245203.

(14) Bera, T. K.; Song, J. H.; Freeman, A. J.; Jang, J. I.; Ketterson, J. B.; Kanatzidis, M. G. Soluble Direct-Band-Gap Semiconductors $LiAsS_2$ and $NaAsS_2$: Large Electronic Structure Effects from Weak As··· S Interactions and Strong Nonlinear Optical Response. *Angew. Chem., Int. Ed.* **2008**, *47*, 7828−7832.

(15) Bera, T. K.; Jang, J. I.; Song, J.-H.; Malliakas, C. D.; Freeman, A. J.; Ketterson, J. B.; Kanatzidis, M. G. Soluble semiconductors $AAsSe_2$ (A= Li, Na) with a direct-band-gap and strong second harmonic generation: A combined experimental and theoretical study. *J. Am. Chem. Soc.* **2010**, *132*, 3484−3495.

(16) Friedrich, D.; Byun, H. R.; Hao, S.; Patel, S.; Wolverton, C.; Jang, J. I.; Kanatzidis, M. G. Layered and Cubic Semiconductors $AGaM'Q_4$ (A^+ = K^+, Rb^+, Cs^+, Tl^+; M'^{4+} = Ge^{4+}, Sn^{4+}; Q^{2-} = S^{2-}, Se^{2-}) and High Third-Harmonic Generation. *J. Am. Chem. Soc.* **2020**, *142*, 17730−17742.

(17) Chen, M.-C.; Wu, L.-M.; Lin, H.; Zhou, L.-J.; Chen, L. Disconnection Enhances the Second Harmonic Generation Response: Synthesis and Characterization of $Ba_{23}Ga_8Sb_2S_{38}$. *J. Am. Chem. Soc.* **2012**, *134*, 6058−6060.

(18) Luo, Z.-Z.; Lin, C.-S.; Zhang, W.-L.; Zhang, H.; He, Z.-Z.; Cheng, W.-D. $Ba_8Sn_4S_{15}$: A Strong Second Harmonic Generation Sulfide with Zero-Dimensional Crystal Structure. *Chem. Mater.* **2014**, *26*, 1093−1099.

(19) Boyd, R. W. *Nonlinear Optics*; Academic Press, 2008.

(20) Campagnola, P. J.; Dong, C.-Y. Second harmonic generation microscopy: principles and applications to disease diagnosis. *Laser Photonics Rev.* **2010**, *5*, 13−26.

(21) Butet, J.; Brevet, P.-F.; Martin, O. J. F. Optical Second Harmonic Generation in Plasmonic Nanostructures: From Fundamental Principles to Advanced Applications. *ACS Nano* **2015**, *9*, 10545−10562.

(22) Petrov, V. Frequency down-conversion of solid-state laser sources to the mid-infrared spectral range using non-oxide nonlinear crystals. *Prog. Quantum Electron.* **2015**, *42*, 1−106.

(23) Chung, I.; Kanatzidis, M. G. Metal Chalcogenides: A Rich Source of Nonlinear Optical Materials. *Chem. Mater.* **2013**, *26*, 849−869.

(24) Chen, H.; Ran, M.-Y.; Wei, W.-B.; Wu, X.-T.; Lin, H.; Zhu, Q.-L. A comprehensive review on metal chalcogenides with three-dimensional frameworks for infrared nonlinear optical applications. *Coord. Chem. Rev.* **2022**, *470*, 214706.

(25) Lin, H.; Wei, W.-B.; Chen, H.; Wu, X.-T.; Zhu, Q.-L. Rational design of infrared nonlinear optical chalcogenides by chemical substitution. *Coord. Chem. Rev.* **2020**, *406*, 213150.

(26) Nikogosyan, D. N. *Nonlinear Optical Crystals: A Complete Survey*; Springer Science, 2005.

(27) Catella, G. C.; Burlage, D. Crystal growth and optical properties of $AgGaS_2$ and $AgGaSe_2$. *MRS Bull.* **1998**, *23*, 28−36.

(28) Zhao, X.; Zhu, S.; Zhao, B.; Chen, B.; He, Z.; Wang, R.; Yang, H.; Sun, Y.; Cheng, J. Growth and characterization of $ZnGeP_2$ single crystals by the modified Bridgman method. *J. Cryst. Growth* **2008**, *311*, 190−193.

(29) Vincenti, M. A.; Gao, J.; de Ceglia, D.; Frantz, J. A.; Scalora, M.; Litchinitser, N. M. Stacked chalcogenide metasurfaces for third harmonic generation in the UV range. *New J. Phys.* **2022**, *24*, 035005.

(30) Gao, J.; Vincenti, M. A.; Frantz, J.; Clabeau, A.; Qiao, X.; Feng, L.; Scalora, M.; Litchinitser, N. M. Near-infrared to ultra-violet frequency conversion in chalcogenide metasurfaces. *Nat. Commun.* **2021**, *12*, 5833.

(31) Zhu, M.; Abdollahramezani, S.; Li, C.; Fan, T.; Harutyunyan, H.; Adibi, A. Broadband-Tunable Third-Harmonic Generation Using Phase-Change Chalcogenides. *Adv. Photonics Res.* **2022**, *3*, 2200064.

(32) Balijapelly, S.; Craig, A. J.; Bin Cho, J.; Jang, J. I.; Ghosh, K.; Aitken, J. A.; Chernatynskiy, A. V.; Choudhury, A. Building-block approach to the discovery of $Na_8Mn_2(Ge_2Se_6)_2$: A polar chalcogenide exhibiting promising harmonic generation signals with a high laser-induced damage threshold. *J. Alloys Compd.* **2022**, *900*, 163392.

(33) Yao, L.; Zeng, Z.; Cai, C.; Xu, P.; Gu, H.; Gao, L.; Han, J.; Zhang, X.; Wang, X.; Wang, X.; Pan, A.; Wang, J.; Liang, W.; Liu, S.; Chen, C.; Tang, J. Strong Second- and Third-Harmonic Generation in 1D Chiral Hybrid Bismuth Halides. *J. Am. Chem. Soc.* **2021**, *143*, 16095−16104.

https://doi.org/10.1021/acs.chemmater.3c01783
Chem. Mater. 2023, 35, 7322−7332

(34) Liu, M.; Quah, H. S.; Wen, S.; Yu, Z.; Vittal, J. J.; Ji, W. Efficient Third Harmonic Generation in a Metal-Organic Framework. *Chem. Mater.* **2016**, *28*, 3385−3390.
(35) Multian, V. V.; Riporto, J.; Urbain, M.; Mugnier, Y.; Djanta, G.; Beauquis, S.; Galez, C.; Gayvoronsky, V. Y.; Le Dantec, R. Averaged third-order susceptibility of ZnO nanocrystals from Third Harmonic Generation and Third Harmonic Scattering. *Opt. Mater.* **2018**, *84*, 579−585.
(36) Mlochowski, J.; Syper, L. *Encyclopedia of Reagents for Organic Synthesis*; John Wiley and Sons Ltd., 2001.
(37) Muenow, D. W.; Margrave, J. L. Mass spectrometric observations of gaseous phosphorus sulfides and oxysulfides. *J. Inorg. Nucl. Chem.* **1972**, *34*, 89−94.
(38) Glenn, J. R.; Cho, J. B.; Wang, Y.; Craig, A. J.; Zhang, J.-H.; Cribbs, M.; Stoyko, S. S.; Rosello, K. E.; Barton, C.; Bonnoni, A.; Grima-Gallardo, P.; MacNeil, J. H.; Rondinelli, J. M.; Jang, J. I.; Aitken, J. A. $Cu_4MnGe_2S_7$ and Cu_2MnGeS_4: two polar thiogermanates exhibiting second harmonic generation in the infrared and structures derived from hexagonal diamond. *Dalton Trans.* **2021**, *50*, 17524−17537.
(39) Kurtz, S. K.; Perry, T. T. A Powder Technique for the Evaluation of Nonlinear Optical Materials. *J. Appl. Phys.* **1968**, *39*, 3798−3813.
(40) Brant, J. A.; Clark, D. J.; Kim, Y. S.; Jang, J. I.; Weiland, A.; Aitken, J. A. Outstanding Laser Damage Threshold in Li_2MnGeS_4 and Tunable Optical Nonlinearity in Diamond-Like Semiconductors. *Inorg. Chem.* **2015**, *54*, 2809−2819.
(41) Dmitriev, V. G.; Gurzadyan, G. G.; Nikogosyan, D. N. *Handbook of Nonlinear Optical Crystals*; Springer Berlin, 1999.
(42) Zhang, J.-H.; Clark, D. J.; Brant, J. A.; Rosmus, K. A.; Grima, P.; Lekse, J. W.; Jang, J. I.; Aitken, J. A. α-Li_2ZnGeS_4: A Wide-Bandgap Diamond-like Semiconductor with Excellent Balance between Laser-Induced Damage Threshold and Second Harmonic Generation Response. *Chem. Mater.* **2020**, *32*, 8947−8955.
(43) Pelant, I.; Valenta, J. *Luminescene Spectroscopy of Semiconductors*; Oxford University Press, 2012.
(44) Hernández, F. E.; Belfield, K. D.; Cohanoschi, I.; Balu, M.; Schafer, K. J. Three- and four-photon absorption of a multiphoton absorbing fluorescent probe. *Appl. Opt.* **2004**, *43*, 5394−5398.
(45) Larsen, J. K.; Donzel-Gargand, O.; Sopiha, K. V.; Keller, J.; Lindgren, K.; Platzer-Björkman, C.; Edoff, M. Investigation of $AgGaSe_2$ as a wide gap solar cell absorber. *ACS Appl. Energy Mater.* **2021**, *4*, 1805−1814.
(46) Kopylov, D. A.; Spasibko, K. Y.; Murzina, T. V.; Chekhova, M. V. Study of broadband multimode light via non-phase-matched sum frequency generation. *New J. Phys.* **2019**, *21*, 033024.
(47) Jackson, A.; Ohmer, M.; LeClair, S. Relationship of the second order nonlinear optical coefficient to energy gap in inorganic non-centrosymmetric crystals. *Infrared Phys. Technol.* **1997**, *38*, 233−244.
(48) Sheik-Bahae, M.; Hutchings, D. C.; Hagan, D. J.; Van Stryland, E. W. Dispersion of bound electron nonlinear refraction in solids. *IEEE J. Quantum Electron.* **1991**, *27*, 1296−1309.

https://doi.org/10.1021/acs.chemmater.3c01783
Chem. Mater. 2023, 35, 7322−7332